Comparison of Secondary Flow Characteristics in Mixed-Flow Turbine between Nozzleless and Symmetric Nozzle Vane Angles under Steady-State Flow at Full Admission

Mohd Jazmi Asyraff Jama'a [1], **Balamurugan Annamalai Gurunathan** [1,*], **Ricardo Martinez Botas** [2] **and Uswah Khairuddin** [3]

1   Department of Mechanical Engineering, Faculty of Engineering, National Defense University of Malaysia, Kuala Lumpur 57000, Malaysia; 3211526@alfateh.upnm.edu.my
2   Department of Mechanical Engineering, Faculty of Engineering, Imperial College London, London SW7 2BX, UK; r.botas@imperial.ac.uk
3   Department of Mechanical Precision Engineering, Malaysia-Japan International Institute of Technology, University of Technology Malaysia, Kuala Lumpur 54100, Malaysia; uswah.kl@utm.my
*   Correspondence: balamurugan@upnm.edu.my

Abstract: In industrial applications, radial or mixed-flow turbines are frequently used in energy recovery systems, small turbines for producing power, and turbochargers. The implementation of radial or mixed-flow turbines helps to maintain high efficiency at a large range of pressure ratios by reducing the overall turbine losses and secondary flow losses. Numerous findings on secondary flow development research adopting double-entry turbines can be obtained in the public domain, except asymmetric volute, which is less well-researched. The focus of the present work is to investigate the evolution of secondary flows and their losses in a mixed-flow turbine used in an asymmetric volute turbine, by employing an experimentally validated three-dimensional computational fluid dynamics (CFD). The flow topology is analyzed to explain the formation and evolution of flow separations at the pressure, suction, and hub surfaces. As the opening angle of the nozzle vane increases, the incidence angle falls into the positive range while the maximum pressure difference between the shroud and hub decreases by about 40%. The results also show that the development of secondary flow accounts for the majority of losses and induced the centrifugal pressure head influence. The presence of symmetric nozzle vanes in both large and small scrolls is also found to have a significant detrimental effect on the turbine efficiency, which is 4% lower than the nozzleless case. Furthermore, significant flow separation is observed in the symmetrical nozzle vane configuration as opposed to that of nozzleless. In addition, the centrifugal pressure head indicated by the maximum pressure difference between the hub and shroud influences the overall turbine efficiency, as the symmetrical nozzle vane arrangement is introduced with two different turbine rotational speeds of 30 K rpm and 48 K rpm.

Keywords: turbocharger volute; asymmetric volute; double-entry volute; symmetric nozzle vanes; secondary flow; losses; centrifugal pressure head

1. Introduction

The use of a turbine in the exhaust flow of a reciprocating engine affects the gas wave dynamics in the exhaust manifold [1]. In a conventional single-entry device, all of the exhaust pipes converge to a single turbine entry, providing a mixing of different flows which depend on valve timing that can have a detrimental influence on the turbine performance. It is feasible to reduce this influence by using a multiple-entry turbine, which is designed to connect exhaust pipes to two or more entries to the turbine volute. The multiple-entry turbine helps the automotive industry boost maximum efficiency. The efficiency of turbines is a key performance parameter to maximize exhaust energy conversion. To achieve

this purpose, it is important to understand the nature and evolution of secondary flows in turbines.

Various researchers [2–13] have used many methods to study the secondary flow development in single-entry turbines under steady flow. Natkaniec et al. [2] initiated a detailed study of secondary flow structure and losses in an asymmetric single-entry turbine with 12 nozzle vanes; they [2] found that corner vortices commonly occurred at the shaft seals while horseshoe vortices occurred at spacers. Then, Chen et al. [3] conducted a study of secondary flow in a nozzleless single-entry turbine by implementing single passage analysis. The latest study on understanding secondary flow development carried out by Yang et al. [4] also involves the single-entry turbine. They observed the formation of flow separations at the pressure, suction, and hub surfaces by analyzing the flow topology on both sides of the blade surfaces. They also suggested that the losses produced by the separations as well as the tip leakage vortex can be identified by calculating the local entropy generation. They concluded that the tip leakage vortex is responsible for the majority of losses (60%), and losses due to the suction surface and induced hub separations are minor. Moreover, the pressure surface separation does not significantly alter the total number of losses but rather redistributes them throughout the blade passage. In addition, other researchers [1,14–18] such as Lin et al. [17] investigated the mechanism of local entropy generation to understand losses in compressible flow through a high-pressure single-entry turbine. They concluded that the entropy generation rate, which is a useful parameter for calculating local and overall losses, is influenced by two main parameters: viscous irreversibility and heat transfer irreversibility.

The influence of the nozzle vane can be seen when Newton [1] carried out an investigation using three different opening vane angles in a double-entry turbine under three different admissions of steady flow and pulsating flow. They found that the steady-state peak efficiency improved by up to 79% with the presence of the largest nozzle throat area. In addition, Simpson et al. [19] studied the loss generation between nozzled and nozzleless configurations in single-entry turbines and found that the horseshoe vortex was resolved at the nozzled volute. However, their prediction indicates that the nozzleless volute, under the same operating conditions, had a smaller loss than the nozzled volute due to a higher level of flow uniformity provided in the nozzleless volute.

Feng et al. [8] conducted a numerical investigation of aerodynamic performance using CFD software by varying the opening vane angle in a single-entry turbine to obtain three different incidence angles of the turbine of 20°, 0°, and −20°. By changing the opening vane angle, the distribution of static surface pressure is affected. The cross-passage vortex has been most highly affected when the incidence angle increases. They concluded that the efficiency drops as the incidence angle increases due to the width of the cross-passage vortex being increased, but the shape of the wake vortex shedding is quite similar for all incidence angles.

In the attempt to improve the effectiveness of the turbocharger turbine in heavy-duty vehicles, the introduction of nozzle vanes such as fixed geometry turbines (FGT) and variable geometry turbines (VGT) are widely used. Researchers [20–24] used the VGT as the alternative method instead of using FGT systems on the double-entry turbine. Dasgupta et al. [23] studied the important aspects of VGT applications on gasoline engines. They [23] concluded that the application of VGT successfully helped to increase the fuel economy, improved transient response and steady state performances, and increased power density. Kreckel et al. [24] carried out the latest CFD investigations on the effect of VGT on the double-entry turbine compared to the single-entry turbines under a steady state. They observed that the pressure separation depends on the degree of the nozzle opening angle where it becomes worse with a smaller opening.

Martinez and Sakai [25] patterned the design of asymmetric double-entry turbines and concluded that the new design will help to optimize the exhaust gas recirculation (EGR). Gurunathan [26] continued the experimental work by using the design of Martinez and Sakai [25] with a nozzleless setting and found that the peak efficiency is up to 78% at a 0.68 velocity ratio. In addition, Gurunathan [26] carried out a further investigation using different nozzle vane arrangements and found that the peak efficiency dropped to 74%. In addition, the inferences by Newton [1] and Gurunathan [26] on turbine performance cannot be compared due to different volute designs. Shah et al. [27] were the first to compare asymmetric and symmetric nozzle vane configurations in the literature. By using the same mixed-flow rotor, inlet duct, and exit duct as the asymmetric design by Gurunathan [26], they [27] were able to develop a symmetric double-entry turbine with the same A/R ratio. At 30 K rpm and 48 K rpm, the asymmetric double-entry turbine [26] performed better, by 2.8% and 8%, respectively, than the novel design of a symmetric double-entry turbine by Shah et al. [27]. In addition, they [27] discovered that an asymmetric double-entry turbine could preserve the distribution of incidence angle at off-design points better than a symmetric double-entry turbine.

The use of double-entry turbines [20–29], especially with asymmetric volute in secondary flow research, is limited compared to single-entry turbines, which have received extensive attention [1–19]. In addition, the influence of nozzle vanes on the secondary flow development and centrifugal pressure head did not achieve much attention in the public domain. To conclude, there is no study investigating the influence of various symmetric nozzle vanes on secondary flow development and centrifugal pressure head influence in asymmetric double-entry volute. In this paper, the asymmetric double-entry volute designed by Martinez and Sakai [25] and the symmetric nozzle vane arrangement by Gurunathan [26] are used to investigate the secondary flow field development. The fluid domain in this simulation is extracted from Gurunathan's [26] 3D CAD model. The analysis of the influence of the centrifugal pressure head in secondary flow under different nozzle vane arrangements is carried out using the validated model. The research question to be addressed in this paper is how the symmetric nozzle vane arrangement influences the centrifugal pressure head and the secondary flow development in an asymmetric double-entry turbine employing a mixed-flow rotor.

2. Methodology

The 3D computational fluid dynamics (CFD) simulation of the asymmetric double-entry turbine volute is validated using the experimental result of Gurunathan [26]. The type of rotor that has been used is a mixed-flow rotor and a mesh sensitivity test is a fundamental step to obtain an optimum mesh number.

2.1. Numerical Setup

To validate simulation results against the experiment, the domains need to consist of a conversion inlet, asymmetric double-entry turbine volute, nozzleless interspace rotor, and outlet that refers to experimental parts by Gurunathan [26]. Figures 1 and 2 show all the CAD models of asymmetric double-entry turbine parts and the full assembly model, respectively. The specifications of the rotor that has been used for the entire simulation is the Rotor A by Abidat [30].

The fluid domain model is generated by extracting the inner surface of the part and changing it into a solid part. The unstructured meshing is employed for the inlet, volute, nozzle interspace, and outlet, while the structured meshing is used for the rotor as shown in Figures 3 and 4, respectively. The mesh generated in the model is a combination of hexahedral, prism, and pyramid mesh elements. Table 1 shows the details of meshing for each fluid domain.
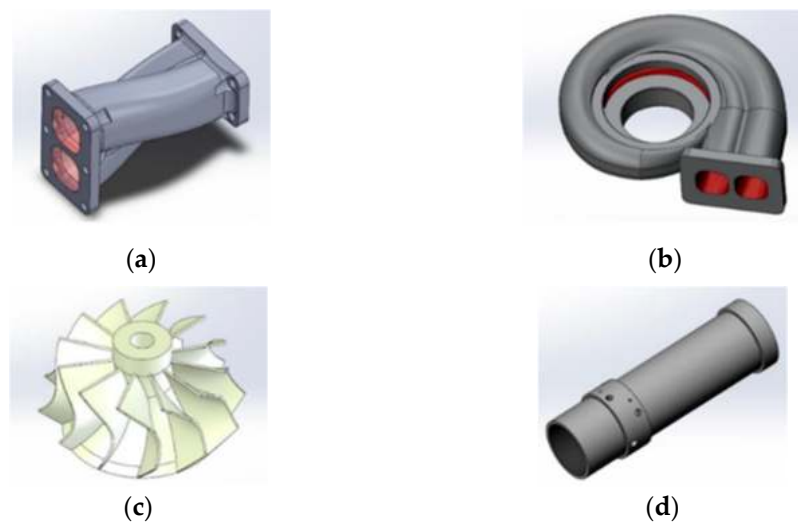
(**a**)　　　　　　　　　　　　　　　　　　　　　(**b**)

(**c**)　　　　　　　　　　　　　　　　　　　　　(**d**)

Figure 1. 3D CAD model of parts [27]. (**a**) Conversion inlet; (**b**) Asymmetric volute with nozzle ring; (**c**) Rotor A; (**d**) Exit duct.
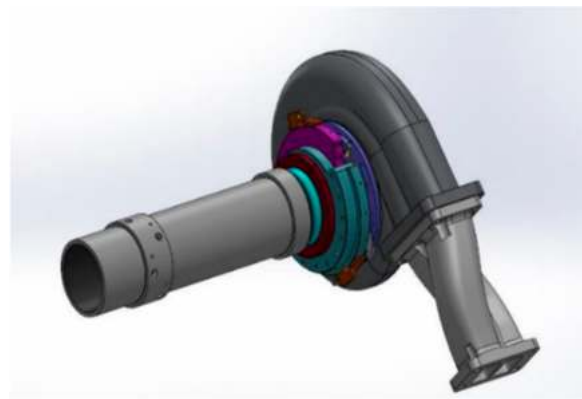

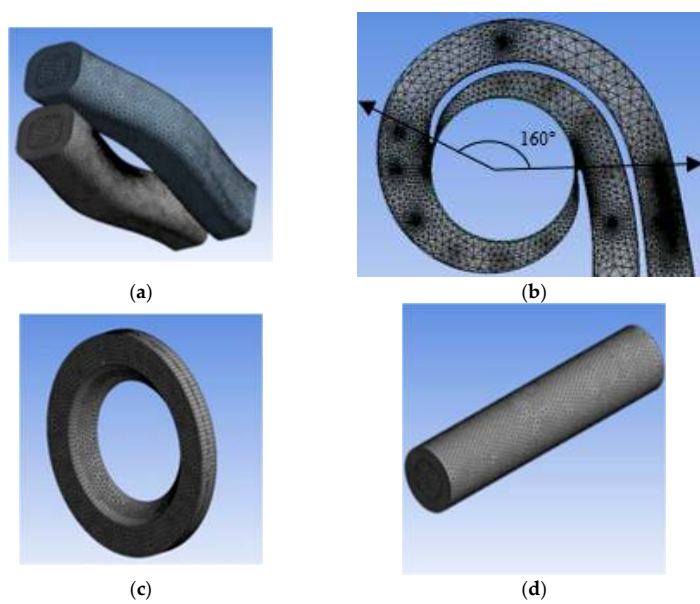**Figure 2.** Full assembly of asymmetric double-entry turbine [27].

(**a**)　　　　　　　　　　　　　　　　　　　　　(**b**)

(**c**)　　　　　　　　　　　　　　　　　　　　　(**d**)

Figure 3. Fluid domain meshes. (**a**) Conversion inlet; (**b**) Asymmetric volute; (**c**) Nozzleless interspace; (**d**) Exit duct.
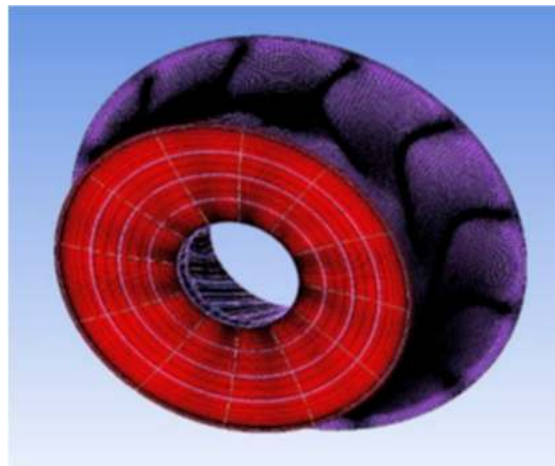
Figure 4. Rotor structured meshing [27].

Table 1. Meshing detail.

Mesh Preference		
Physics preference	CFD	
Solver preference	CFX	
Relevance center (mesh size)	Fine	
Type of mesh	Hexahedral, prism, and pyramid	
Face sizing	Inlet face and outlet face	
Inflation	Boundary scoping method; all faces except inlet and outlet face	
Domains details		
Type of mesh	Unstructured	
Domain	Total nodes	Total elements
Inlet duct	37,656	89,421
Asymmetric volute	274,931	742,788
Nozzleless vane	13,192	30,740
Nozzled vane S51L51	513,776	1,649,801
S66L66	524,889	1,698,116
S71L71	507,153	1,629,192
Exit duct	25,323	70,489
Structured		
Rotor	307,278	281,736

The general interface is set between every domain except interfaces between nozzleless to rotor and rotor to outlet where the interfaces are set to stage (mixing plane) option. This is due to the nozzleless and outlet domains being connected to the rotating domain (rotor) where the effect of transient between domains is considered. The equation of the standard k-epsilon (k-ε) turbulent model is used in this simulation where the model is known due to its wide applications in the turbulence flow. The prediction of turbulent flow to analyze turbocharger performance by using this turbulent model is accurate as mentioned by Palfreyman [31].

2.2. Boundary Conditions

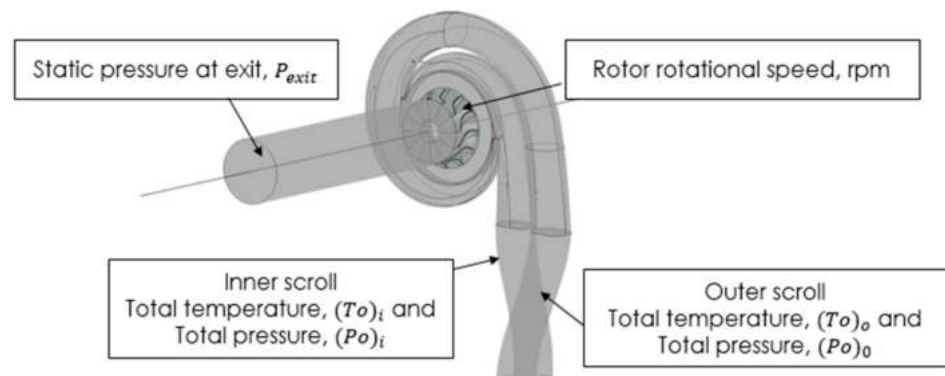Figure 5 shows the locations for the boundary conditions for the entire simulation.

Figure 5. Boundary conditions' location.

2.3. Solver Setting

Three different numbers of iterations (400, 1000, and 2000) are investigated to achieve the smallest number of iterations for the solution to converge when all the convergence criteria are met. The convergences criterion being monitored are momentum and mass, heat transfer, turbulence, efficiency, and torque. The convergence residual is set as RMS residual type (1×10^{-7}). Since the solution of the equations starts to converge and remain steady after 400 iterations, 400 iterations have been used in all the simulations in this research.

2.4. Turbomachinery Performance Parameters

Parameters such as mass flow rate, total inlet and outlet pressure, total inlet and outlet temperature, and exit static pressure are obtained in this post-processing. These parameters are substituted into Equations (1) and (4) to measure turbine performance.

The total to static efficiency as given by Equation (1) can be defined as the ratio of actual work to isentropic work for both scrolls where the subscript *i* represents the inner scroll while subscript *o* represents the outer scroll. In the double-entry turbine, Equation (2), which represents the actual shaft power measurement, remains the same as that of a single-entry.

$$\eta ts = \frac{\dot{W}_{act}}{\left(\dot{W}_{IS}\right)_i + \left(\dot{W}_{IS}\right)_o} \tag{1}$$

$$\dot{W}_{act} = \frac{2\pi NT}{60} \tag{2}$$

where *N* is the turbine rotational speeds and *T* is the torque of the turbine. The isentropic power is measured for both inlets as given by Equation (3).

$$\dot{W}_{IS} = \dot{m}Cp(T_0)\left(1 - \left(\frac{P_7}{P_0}\right)^{\frac{\gamma-1}{\gamma}}\right) \tag{3}$$

where $\dot{m}$ is the mass flow rate, Cp is the specific heat of the gas at constant pressure, T_0 is the total temperature at the inlet, P_7 is the static pressure at the exit, P_0 is the total pressure at the inlet, and γ is the specific heat ratio.

The velocity ratio is the ratio of the blade speed to isentropic absolute flow velocity, and is given in Equation (4).

$$VR = \frac{\pi D_5 \left(\frac{N}{60}\right)}{\sqrt{2\left(\frac{\left(\dot{W}_{IS}\right)_i + \left(\dot{W}_{IS}\right)_o}{\dot{m}_i + \dot{m}_o}\right)}} \tag{4}$$

where D_5 is the rotor's mean inlet diameter.

Based on these two equations (Equations (1) and (4)), the plot of the total to static efficiency versus velocity ratio can be obtained. In addition, the overall mass flow parameter is defined in Equation (5).

$$MFP = \frac{(\dot{m}_i + \dot{m}_o)\sqrt{T_0}}{P_0}$$

(5)

where the value of the overall temperature T_0 and overall pressure P_0 are given in Equations (6) and (7), respectively,

$$T_0 = \frac{\dot{m}_i(T_0)_i + \dot{m}_o(T_0)_o}{\dot{m}_i + \dot{m}_o}$$

(6)

$$P_0 = \frac{(P_0)_i(\dot{W}_{is})_i + (P_0)_o(\dot{W}_{is})_o}{(\dot{W}_{IS})_i + (\dot{W}_{IS})_o}$$

(7)

and the overall pressure ratio is given in Equation (8),

$$PR = \frac{PR_i(\dot{W}_{is})_i + PR_o(\dot{W}_{is})_o}{(\dot{W}_{IS})_i + (\dot{W}_{IS})_o}$$

(8)

where the pressure ratio for each scroll, PR_i, is inner pressure ratio and PR_o is outer pressure ratio, which are given in Equations (9) and (10), respectively,

$$PR_i = \frac{(P_0)_i}{P_7}$$

(9)

$$PR_o = \frac{(P_0)_o}{P_7}$$

(10)

Based on these two equations (Equations (5) and (8)), the plot of the overall mass flow parameter versus pressure ratio can be obtained.

2.5. Numerical Validation

The boundary conditions, as shown in Tables 2 and 3, that are being used for validation are nozzleless configurations at both 30 K rpm and 48 K rpm, obtained by Gurunathan [28] through experimental work. The performance characteristics comparison between simulation and experiment is shown in Figures 6 and 7.

Table 2. Operating conditions for validation at 30 K rpm.

Boundary Conditions						
Rotational speed (rpm)		30,049.4	29,838.9	29,323.3	29,901.2	29,839.9
Total pressure (Pa)	Inner scroll	162,733.4	112,004.5	123,634.2	116,257.0	112,004.5
	Outer scroll	162,800.7	111,510.5	123,587.5	116,373.7	111,510.5
Total temperature (K)	Inner scroll	338.4	332.1	334.5	332.9	332.1
	Outer scroll	337.7	331.7	334.4	332.6	331.7
Exit Pressure (Pa)		100,009.1	100,078.1	100,069.4	99,980.2	100,078.1

Table 3. Operating conditions for validation at 48 K rpm.

Boundary Conditions						
Rotational speed (rpm)		48,615.7	46,865.6	48,411.4	47,799.2	48,027.9
Total pressure (Pa)	Inner scroll	185,527.0	159,079.3	144,041.9	137,844.7	127,505.8
	Outer scroll	184,903.2	158,589.4	143,795.0	138,110.4	127,444.2
Total temperature (K)	Inner scroll	334.8	331.4	331.8	336.7	333.7
	Outer scroll	334.5	331.0	331.2	336.4	333.4
Exit Pressure (Pa)		100,122.9	100,074.0	100,076.3	100,047.6	100,048.6
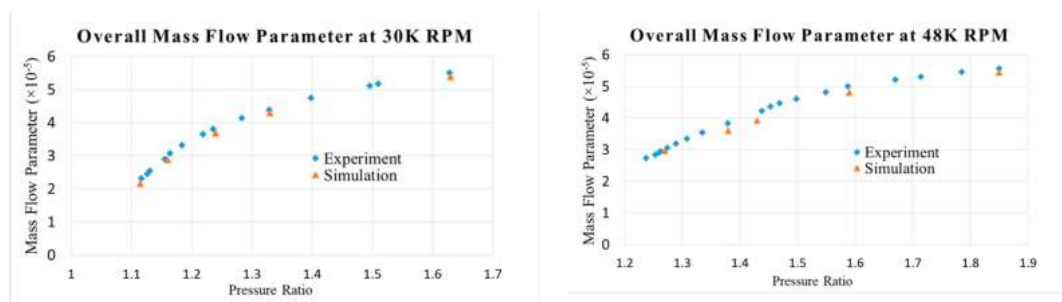
Figure 6. Overall mass flow parameter versus pressure ratio of 30 K rpm and 48 K rpm.
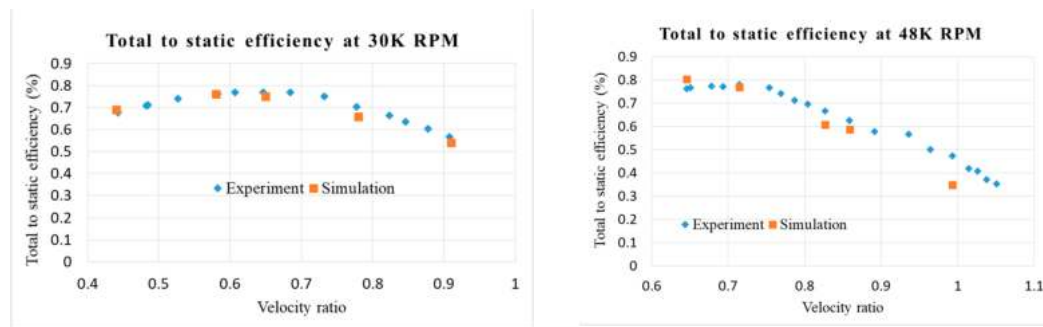
Figure 7. Total to static efficiency versus velocity ratio of 30 K rpm and 48 K rpm.

The overall root mean square of the deviation recorded between simulation and experimental data for both mass flow parameters and total to static efficiency at 30 K rpm are 4% and 2.5%, respectively, while at 48 K rpm they are 4.4% and 7.4%, respectively. It can be seen that the simulation mass flow parameter and total to static efficiency have the same trend as the experiment. It is worth noting that the rotor torque in CFD is extracted by integrating the pressure force over the blade surfaces, whereas in the experiment, the torque is directly measured via a load cell fixed on the body of the eddy-current dynamometer. To sum up, all the results for validation show good agreement between the experiment and simulation for speeds of both 30 K rpm and 48 K rpm.

2.6. Mesh Independence Study

A mesh-sensitivity test is carried out for the rotor domain to ensure that the flow structures of interest to the study are accurately captured, such as tip leakage vortex or horseshoe vortex at the rotor passage blade. Eight different mesh numbers are investigated in this test, as shown in Table 4. The mesh numbers are increased until the total to static efficiency and velocity ratio remained unchanged within ±5 percent.

Table 4. Mesh sizes.

Target Passage Mesh Sizes	Node Count
Coarse	20,000
Medium	150,000
Fine	250,000
Specify	200,000
	300,000
	350,000
	400,000
	500,000

The total to static efficiency versus mesh numbers graph observed in the mesh sensitivity test is shown in Figure 8. The highest peak of total efficiency of 78.4% is recorded at 200,000, 250,000, 300,000, and 350,000 mesh numbers. The final mesh number that has been adopted in this research for the rotor is 200,000 nodes because the velocity ratio of 0.627 remains constant with a deviation of two points percentage and the total to static efficiency becomes stable as the mesh number increase.
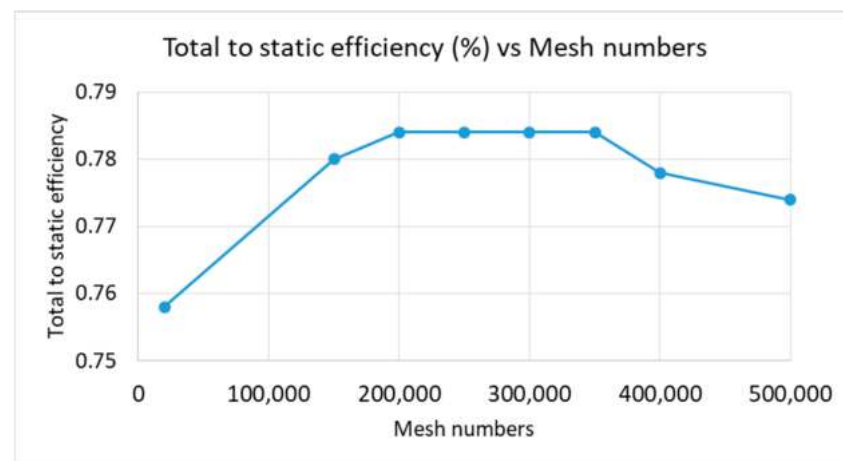
Figure 8. Graph of the total to static efficiency versus mesh numbers.

3. Performance Analysis

Table 5 shows the list of configurations that are being investigated for this current paper.

Table 5. List of configurations.

Vane Angle in Inner Scroll Circumference	Vane Angle in Outer Scroll Circumference	Configuration
Nozzleless	Nozzleless	Nozzleless
51	51	S51L51
66	66	S66L66
71	71	S71L71

3.1. Design Point

The nozzleless turbine is the chosen configuration to be the baseline among other configurations shown in Table 5. The absence of skin friction loss in the nozzleless configuration is the primary reason for the latter being selected as the baseline model. Figure 9 shows the fluid domains of the nozzleless and nozzled configurations.
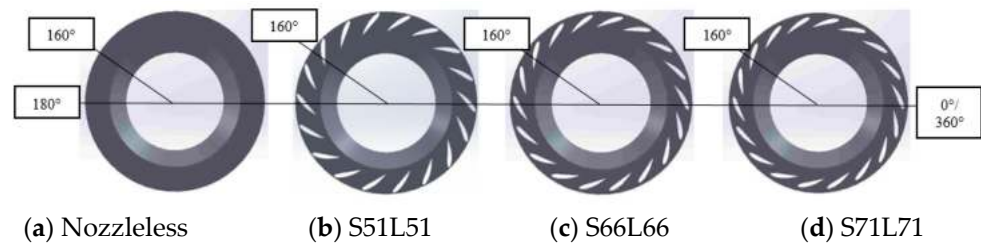
(**a**) Nozzleless   (**b**) S51L51   (**c**) S66L66   (**d**) S71L71

Figure 9. Nozzleless and nozzled configuration.

The flow field analysis is carried out through the entire simulation using the flow entering the chosen rotor passage. The distribution of incidence angle and entropy generation are being examined to select the proper passage for analysis. In the nozzleless and symmetric (S66L66) configuration, the incidence angle at 30 K rpm is recorded at $-12°$ and $-4°$, respectively. Figure 10 shows the incidence angle distribution across the periphery of the turbine at a specific spanwise of 0.4 for both configurations. It demonstrates a uniform distribution for each rotor passage with a deviation of 1% average incidence angle for both configurations.
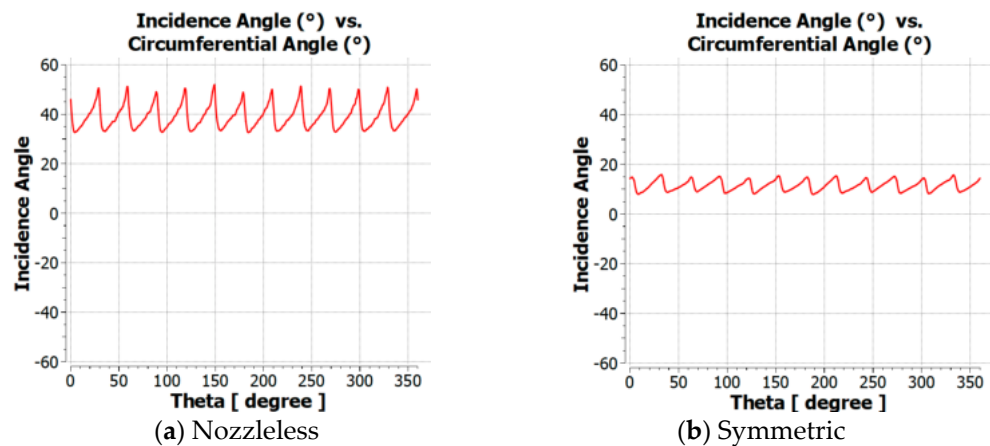

(**a**) Nozzleless   (**b**) Symmetric

Figure 10. Incidence angle plot across the circumferential.

Figure 11 shows the entropy generation distribution in both nozzleless and symmetric configurations where it has quite the same level of fluctuation because of the uniformity of the flow entering the rotor passage blade. Thus, the continuation of the loss distribution can be investigated by using a single passage analysis for the nozzleless and symmetric configuration. The passage between blades 2 and 3 is chosen randomly for the secondary flow analysis through the entire simulation, as shown in Figure 12.
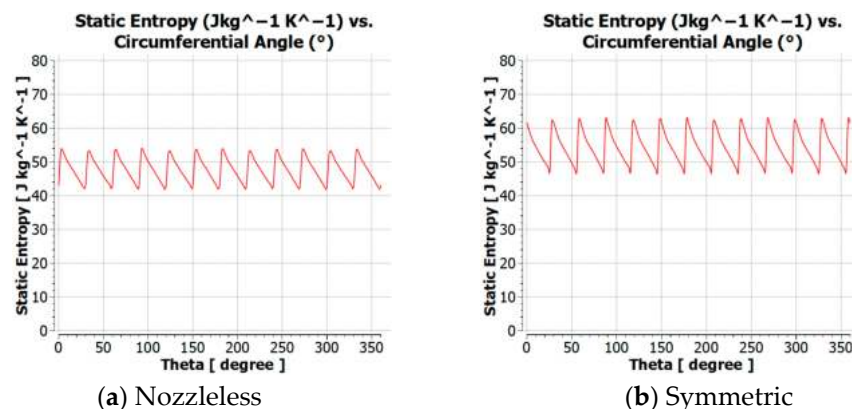

(**a**) Nozzleless   (**b**) Symmetric

Figure 11. Distribution of entropy generation across the rotor circumferential.
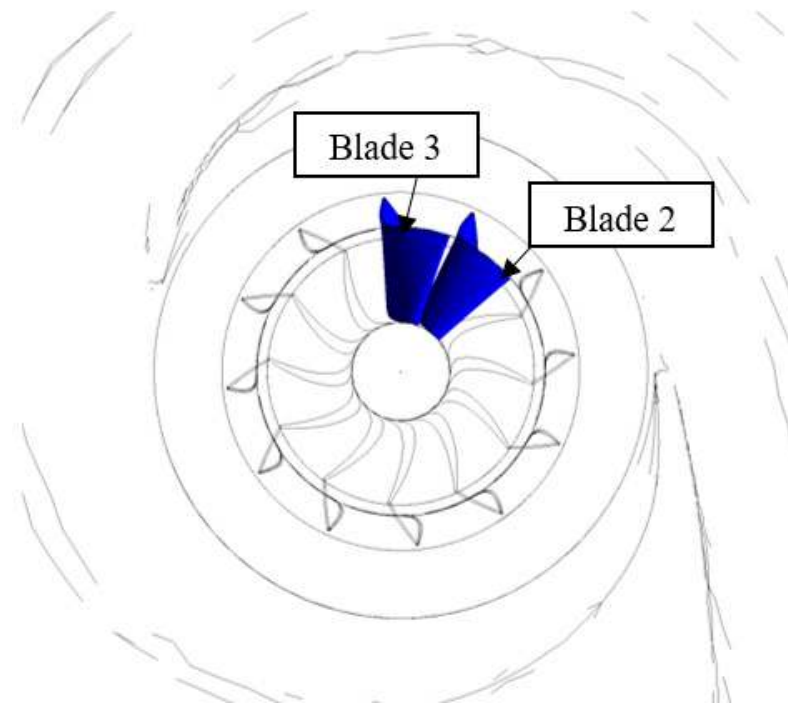
Blade 3

Figure 12. Location of blades.

In the nozzleless configuration, the volute is responsible for maintaining the swirl component of the flow while setting the flow angle at the rotor inlet. With the absence of a nozzle vane in a nozzleless configuration, the reduction of skin friction loss helps in guiding the flow into the rotor without any power loss.

The flow field predicted by the peak efficiency point of nozzleless configuration is studied first. The contour plot of reduced pressure on both pressure and suction surfaces with the lines of wall shear stress is presented in Figure 13, where the significant influence of secondary flow from the reduced pressure perspective is shown. From the leading edge of the blade on the hub surface, as illustrated in Figure 14, it is possible to see that the flow moves from the pressure surfaces towards the suction surface and trails the passage pressure gradient with no obvious trace of separation. On the pressure surface, it can be observed that the reduced pressure gradient is favorable close to the leading edge and an attachment line is formed near the shroud side and the rest of the flow is moving from the leading edge to the trailing edge smoothly. The reduced pressure gradient upstream of feature A acts to drift the friction lines formed into an attachment line to the shroud surfaces indicating significant proof of the tip leakage as reported by many researchers on the axial turbine blade. Feature A shows the focus point near the leading edge of the shroud side. However, on the suction surface, some of the critical points such as focus, saddle points, and attachment nodes are located clearly. The attachment node at the hub side of the suction surface indicates the horseshoe vortex development is taking place there. The flow is moving upwards towards the shroud side blending with the tip leakage vortex friction lines. The flow topology on the suction surface as illustrated in Figure 13b shows a saddle point located near the leading edge of the 90% blade span representing the tip leakage flow drifted from the pressure surface. It is also noted that separations occur on the suction surface.
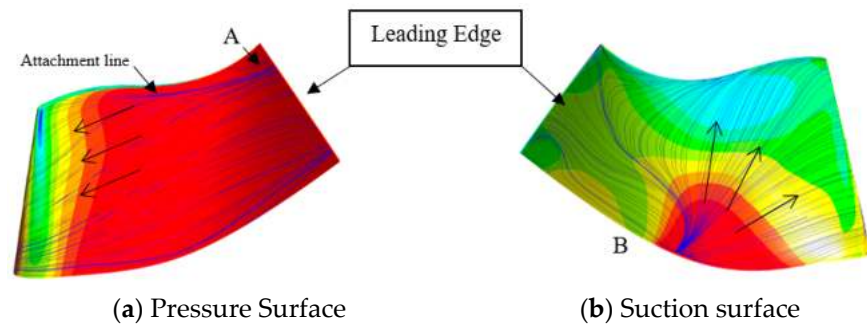
(**a**) Pressure Surface   (**b**) Suction surface

Figure 13. 30 K rpm flow topology at the rotor blade surfaces of nozzleless configuration.
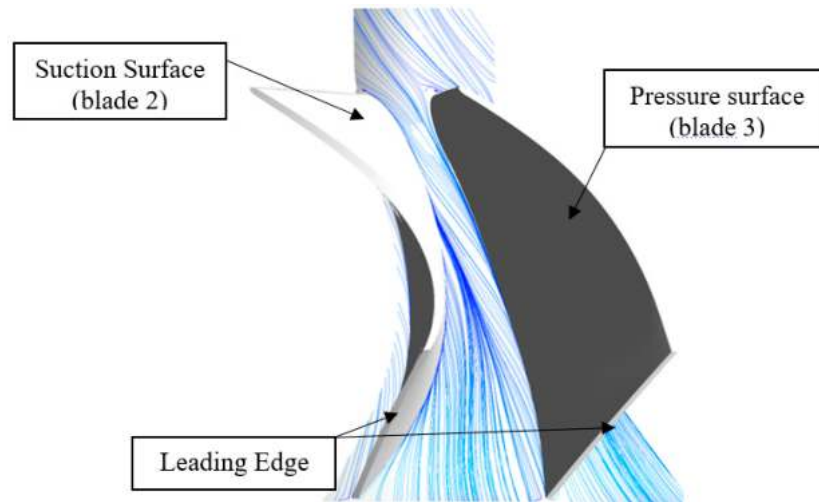

Figure 14. Hub surface of nozzleless configuration at 30 K rpm.

Figure 15 shows the flow near the shroud predicted by the number of particles released at the leading edge of the rotor passage at 90% of the blade span. The strength of the tip leakage vortex indicated by Feature A is seen in this plot, where it peaks at 50% of the blade chord. In addition, Feature B, which characterizes the shroud side passage vortex, is also clearly seen in this plot as it is possible to see the movement of fluid from the pressure surface across the passage to the suction surface.
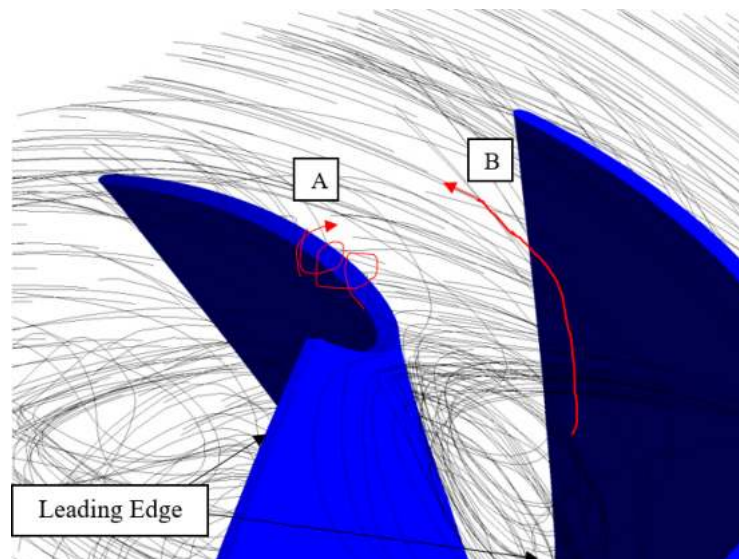

Figure 15. Path lines predicted at 90% of blade span of nozzleless configuration at 30 K rpm.

This operating condition with the incidence angle of the flow entering the rotor passage at $-12°$, almost favorable degree of incidence angle, results in a fairly orderly flow field that follows the blade curvature on the pressure side of the blade, as shown in Figure 16. As a consequence, low levels of loss in the pressure surface are seen when compared to that associated with the suction surface. The tip leakage vortex which is fed by the flow moving up in a positive spanwise at the leading edge is demonstrated in Figure 17, which shows a cross-section passage at 50% of the blade chord. In Figure 16b, there is a region where high entropy generation is detected at the shroud side where the development of tip leakage vortex occurs. Some of the flow leaks over the blade tip from the pressure side to the suction side; this creates a strong tip leakage vortex on the pressure side of the tip section. This tip leakage vortex stretches the entire length of the blade chord and the remainder of the flow moves down to the hub side of the suction surface. This flow also creates another area of entropy generation in the hub region of the suction surface known as the horseshoe vortex, but this is not as strong as the tip leakage vortex.
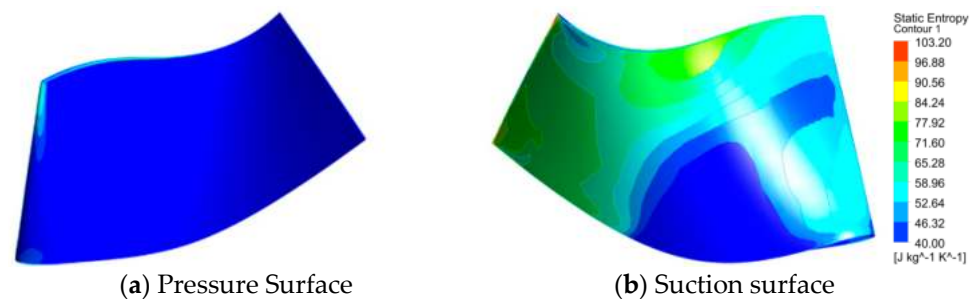

(**a**) Pressure Surface   (**b**) Suction surface

Figure 16. 30 K rpm entropy generation at both surfaces of nozzleless configuration.
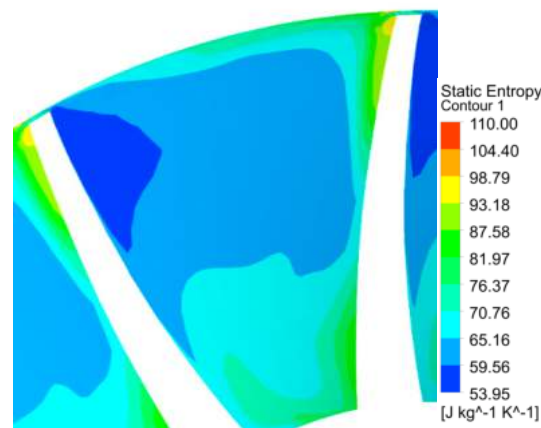

Figure 17. Entropy generation contour plot at cross-section 50% of rotor passage span.

The maximum pressure difference between the shroud and hub side is used in this simulation to indicate the strength of the centrifugal pressure head at the rotor inlet. Nozzleless configuration records a maximum pressure difference of 1.048 kPa.

As the symmetric nozzle vane is introduced, the role of the volute in determining the flow angle entering the rotor inlet has been transferred to nozzle vanes. S66L66 configuration will be used to analyze the flow field and secondary flow owing to its highest peak efficiency amongst all symmetric configurations. The flow topology at both the pressure and suction surfaces of the blade for S66L66 is presented in Figure 18. Theoretically, the S66L66 has a small negative incidence angle of $-4°$, which tends to create the flow separation which is more significant at the pressure surface compared to the suction surface. This is verified by a critical point and two attachment lines located at the pressure surface, as shown in Figure 18a. In addition, the occurrence of critical point and attachment lines is more significant in the nozzled configuration than the nozzleless configuration. The

concentration of attachment lines (Position 1) near the shroud side is stronger than the nozzleless configuration, which is caused by the critical point (Feature A) at the tip of the leading edge. The attachment lines also terminate near 80% streamwise, similar to nozzleless configurations. Hence, the attachment lines (Position 2) near the hub side suggest that the flow has a separation due to the weak horseshoe vortex which can be seen up through 50% streamwise. For the flow field at the suction surface, the concentration of flow separation is weaker than that of the nozzleless configuration. A saddle point (Feature B) located at 20% blade span near the leading edge produces attachment lines near the shroud side (Position 3). Concisely, the flow in symmetric configuration tends to separate at both blade surfaces and is more significant at the pressure surface as opposed to the nozzleless configuration where the flow separation is more significant at the suction surface.
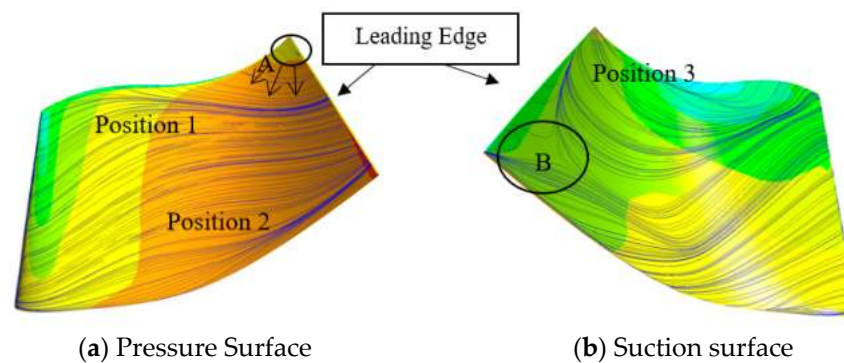

(**a**) Pressure Surface　　　　　　　　(**b**) Suction surface

Figure 18. 30 K rpm flow topology at the rotor blade surfaces of S66L66 configuration.

The flow on the hub surface has the same pattern with a nozzleless configuration as in a symmetric configuration, as shown in Figure 19, where the flow moves from the pressure surfaces to the suction surfaces, but with a high concentration of flow from the leading edge to 50% of the blade chord. Furthermore, no distinct flow separation is seen there.
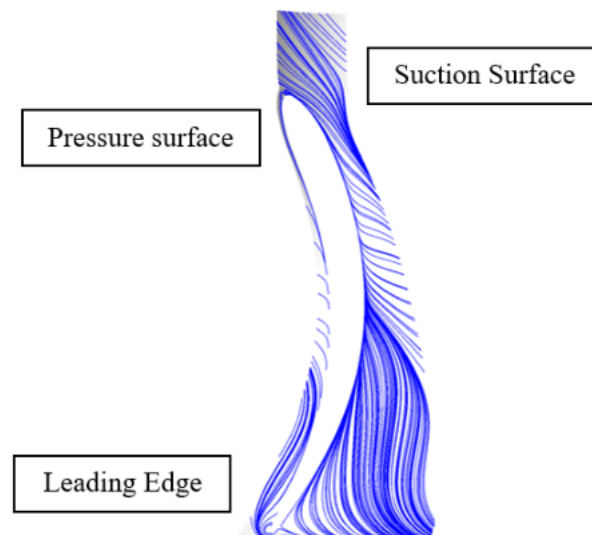

Figure 19. Hub surface of S66L66 configuration at 30 K rpm.

At 90% blade span, the development of the tip leakage vortex is stronger with a higher concentration of recirculating flow (Feature A) than the nozzleless configuration. In addition, the inflow vortex (Feature B) shows a stronger concentration located near the suction surface. The strong recirculation flow is induced by the attachment lines located at both the shroud side of the pressure and suction surfaces, as shown in Figure 20.
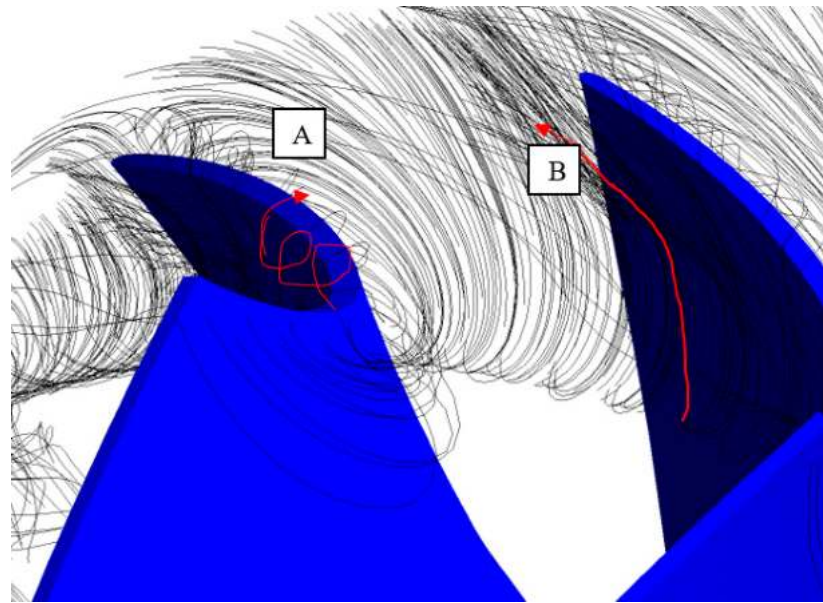
Figure 20. Path lines predicted at 90% of blade span of S66L66 configuration at 30 K rpm.

The flow topology at S66L66 has clearly shown the existence of tip leakage vortex and horseshoe vortex development. The entropy generation, as shown in Figure 21, verifies the occurrence, with a bigger area of high entropy spotted at the suction surface where it is more significant than the nozzleless configuration. The development of a tip leakage vortex and cross passage at the suction surface become stronger caused by the critical points where the flow separation becomes more significant after 50% of the blade chord at the suction surface. The tip leakage vortex, which is fed by the flow moving up in a positive spanwise at the leading edge, and the cross-passage vortex are demonstrated in Figure 22, which shows a cross-section passage of entropy generation at 60% of the blade chord where it seems the higher entropy located only at the suction surface. In addition, the horseshoe vortex induced by Feature B in Figure 18 has created some regions with high entropy near the hub side of the suction surface, which is more significant than the nozzleless configuration.

The presence of a symmetric nozzle vane in the nozzle interspace has affected the maximum pressure difference between the hub and shroud. The secondary flow development in symmetric configuration changes the magnitude of pressure difference to 1.5 kPa, which is 50% more than the nozzleless configuration.
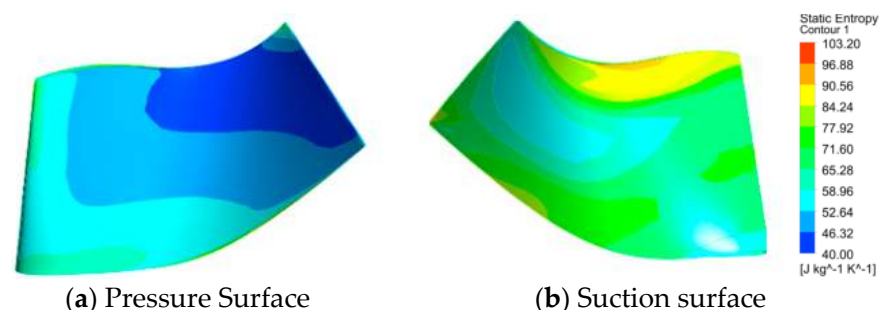

(**a**) Pressure Surface   (**b**) Suction surface

Figure 21. 30 K rpm entropy generation at both surfaces of S66L66 configuration.
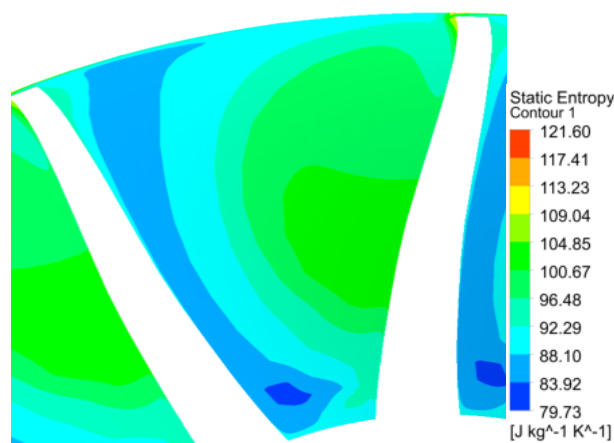
Figure 22. Entropy generation contour plot at cross-section 60% of rotor passage span.

The symmetric opening vane angle has been an important factor that influences the overall turbine efficiency where the total to static efficiency difference between nozzleless and nozzleless turbines is significant. S71L71 has the smallest opening vane angle compared to S66L66 and S51L51. The difference in flow topology as the nozzle vane closes in symmetric configurations is shown in Figure 23. As the nozzle vane opens from S71L71 to S66L66, the attachment lines shift towards both the shroud and hub side at the pressure surface and the focus point at the tip of the leading edge becomes more significant and the attachment lines at the shroud side of the suction surface have a bigger area coverage due to the strong tip leakage vortex. Moreover, as the nozzle vane opens from S66L66 to S51L51, the concentration of attachment lines at the pressure surface becomes significant with a bigger focus point and the attachment lines at suction surfaces have stretched through the trailing edge.

(**a**) S51L51   (**b**) S66L66   (**c**) S71L71
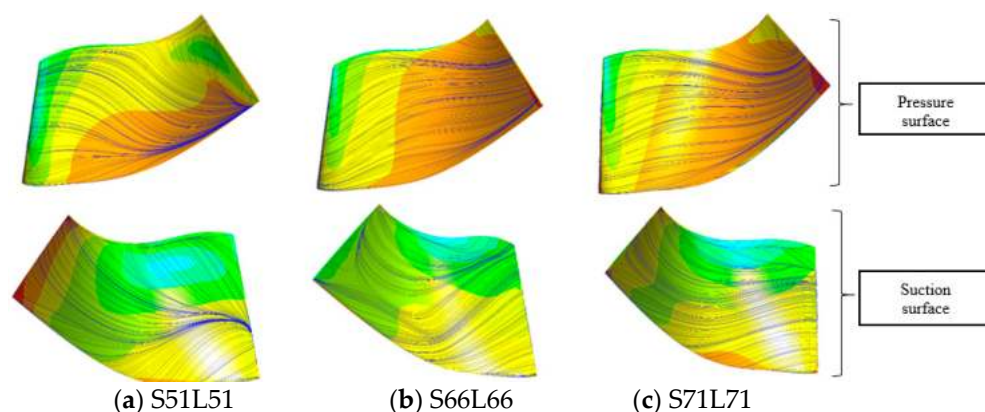
Figure 23. Flow topology at symmetric configurations.

Entropy generation is the best parameter to consider in evaluating losses due to the flow separation as the opening vane angle increases. This is shown in Figure 24. As the nozzle vane opens from S71L71 to S66L66, the magnitude of entropy generation at the shroud side of the suction surface decreases and it spreads across the surface. However, as the nozzle vane opens from S66L66 to S51L51, the area of high entropy generation at the shroud side is more significant with a larger area of high intensity across the surface.

(**a**) S51L51   (**b**) S66L66   (**c**) S71L71

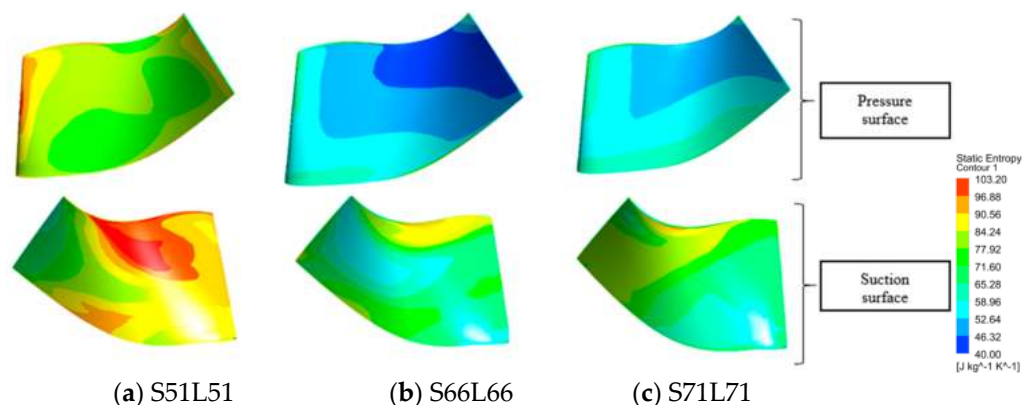**Figure 24.** Entropy generation at symmetric configurations.

In addition, from the centrifugal pressure head perspective, the maximum pressure difference has a changing trend as the nozzle vane closes as shown in Table 6. As the nozzle vane opens from S71L71 to S66L66, the centrifugal pressure head has a decreasing trend, as opposed to the nozzle vane opening from S66L66 to S51L51. This is due to S66L66 having the weakest flow separation that indicates the lowest losses, resulting in the lowest centrifugal pressure head while S51L51 has the strongest flow separation with a higher number of attachment lines and critical points. On the other hand, S71L71 has a mild flow separation, which is stronger than S66L66, but weaker than S51L51.

Table 6. Maximum pressure difference at symmetric configurations for both speeds.

Configuration	Rotational Speed (rpm)	Incidence Angle (°)	Maximum Pressure Difference (Pa)	Total to Static Efficiency (%)
S51L51	30 K	−57.9	2690	60.0
	48 K	No experimental data		
S66L66	30 K	−4	1571	70.4
	48 K	−25	1806	74.0
S71L71	30 K	8	1808	68.8
	48 K	−2	2034	72.0

The concentration of flow separation at pressure and suction surfaces increases as the opening vane angle increases. Furthermore, as the nozzle vane opens, the magnitude of entropy generation increases and is located at the shroud side only.

As the turbine rotational speeds increase from 30 K rpm to 48 K rpm, the flow topology for all configurations changes. As in nozzleless configuration, the flow tends to separate at both sides of the suction and pressure surface. On the pressure surface, it can be observed that the reduced pressure at the leading edge does not have a smooth gradient compared to 30 K rpm because the strength of the centrifugal pressure head is stronger as rotor speed increases. In addition, an adversely reduced pressure gradient can be seen near the attachment lines. At the hub side, the reduced pressure gradient acts to drift the friction lines upwards to form an attachment line at the shroud surfaces showing significant proof of the horseshoe vortex, known as the hub-side passage vortex. On the other side of the suction surface, two separation lines are located near the trailing edge of the 40% blade span where the development of the horseshoe vortex is weaker as turbine speeds increase. In summary, the flow still separates at both surfaces but with the least critical points and fewer attachment lines as the turbine speeds increase.

With the presence of symmetric nozzle vanes of 66° (S66L66 configuration), the flow only separates at the pressure surface of the blade as the turbine speeds increase. The attachment lines on the pressure surface are still noticeable but with a weaker concentration.

There is only one focus point located at the leading edge of the shroud side as the turbine speeds increase.

Generally, the flow in the nozzleless configuration has the least separation compared to the nozzled configurations as the turbine speed increases. Figures 25 and 26 show the difference in flow topology between nozzleless and all symmetric nozzle configurations at both turbine speeds of 30 K rpm and 48 K rpm, respectively. At 30 K rpm, as the symmetric nozzle vane is introduced, the flow topology becomes slightly different at both surfaces compared to the nozzleless configuration, in which at least three attachment lines and two critical points are observed. On the other hand, when the nozzle vanes are introduced into the nozzle interspace at 48 K rpm, the flow tends to separate at the pressure surface only as opposed to the nozzleless configuration where it separates at both sides of pressure and suction surfaces. In addition, the concentration of flow separation at 48 K rpm is weaker than 30 K rpm with a maximum of two attachment lines and a single focus point noticed.
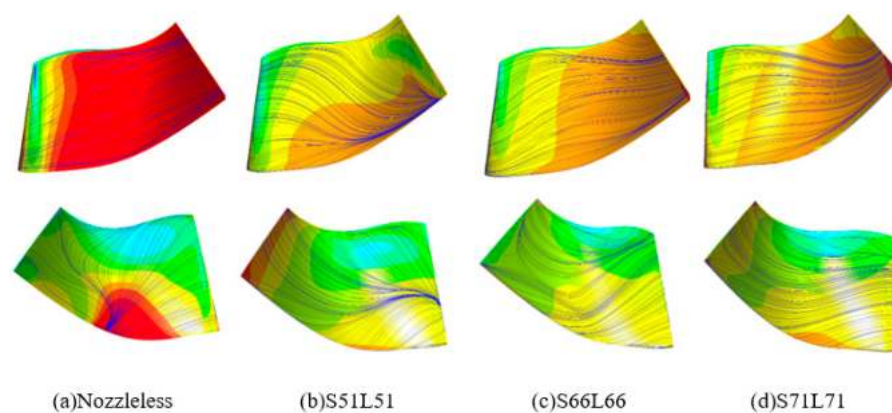

Figure 25. 30 K rpm flow topology.
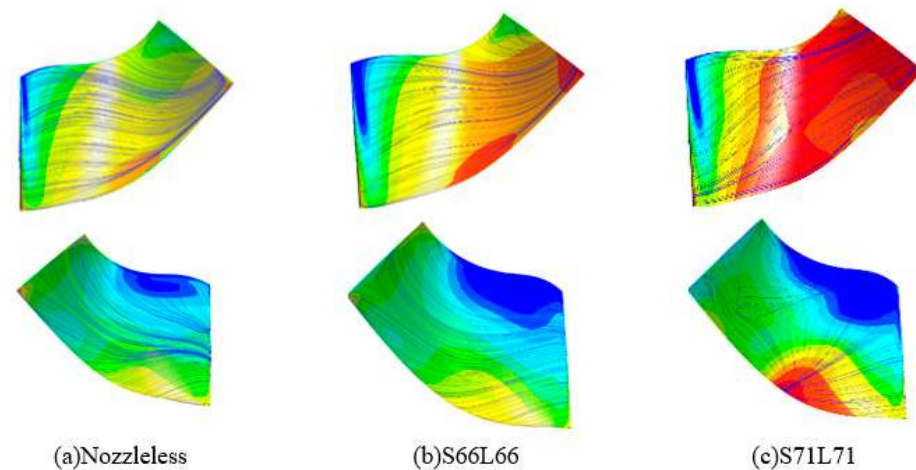
Figure 26. 48 K rpm flow topology.

From the symmetricity perspective, as the nozzle vane opens from S71L71 to S66L66 at 48 K rpm, the attachment lines at the pressure surface are thinner than 30 K rpm at suction surfaces, and the attachment line diminishes, while the focus point near the leading edge of the pressure surface is still observed at both 30 K rpm and 48 K rpm. In conclusion, the influence of symmetricity on the flow separation is the same but with lower intensity as the turbine speed increases.

From the entropy generation perspective, a distinct difference is observed as the turbine speed increases where the magnitude of entropy generation at both pressure and suction surface changes. Figures 27 and 28 show the difference in entropy generation between nozzleless and all symmetric configurations for turbine speeds of 30 K rpm and 48 K rpm, respectively.
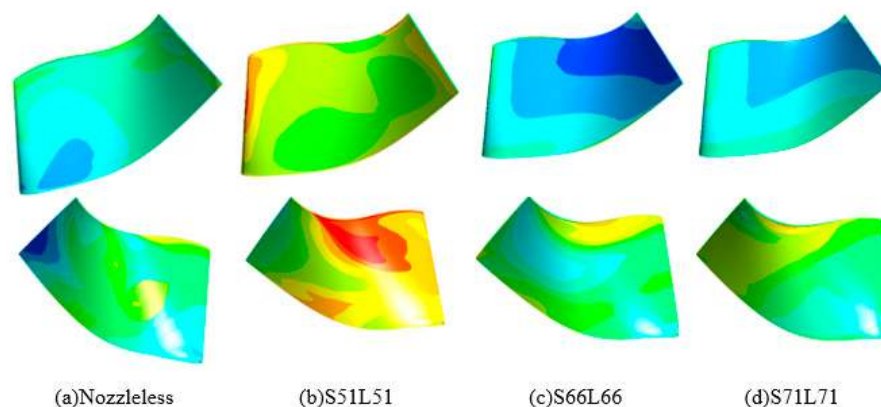
Figure 27. 30 K rpm entropy generation.
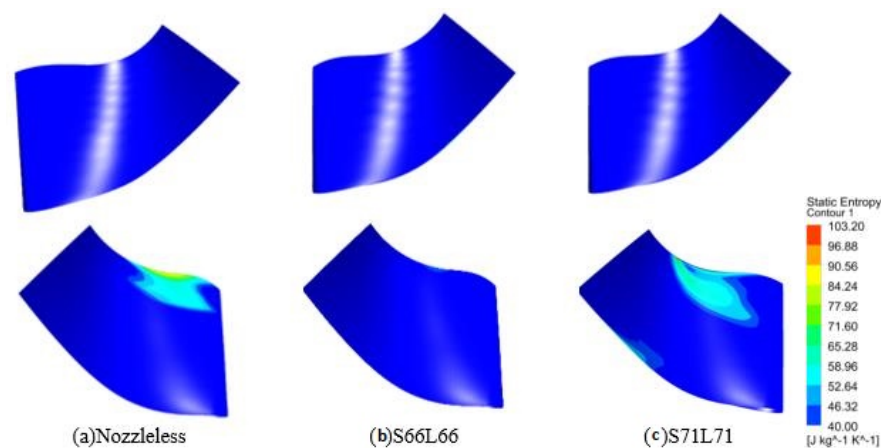
Figure 28. 48 K rpm entropy generation.

In the nozzleless configuration, the magnitude of entropy generation at both pressure and suction surface is reduced significantly as the turbine speed increases from 30 K rpm to 48 K rpm. In addition, the region of high entropy generation is only located at the shroud side of the suction surface. Meanwhile, with the presence of a symmetric vane angle of 66° (S66L66), low entropy generation at both scrolls is spotted as turbine speed increases. However, the region of high entropy generation at the suction surface is much smaller than the nozzleless configuration as turbine speed increases.

As the nozzle vanes are introduced into the turbine at 30 K rpm, the entropy generation significantly increases at both surfaces and becomes more pronounced near the shroud side of the suction surface. However, as turbine speed increases to 48 K rpm, the region and magnitude of entropy generation are smaller, especially at the suction surface.

From the symmetricity perspective, as the nozzle vane closes from S66L66 to S71L71 at 30 K rpm, the region of entropy generation at the shroud side of the suction surface grows bigger while a small deviation happens at the pressure surface. As the turbine speed increases to 48 K rpm, the same pattern of entropy generation occurs but with low intensity where there is only one spike of entropy generation spotted at the shroud side of the suction surface. In summary, S66L66 has the smallest region of high entropy indicating the least losses at both turbine speeds among other symmetric configurations.

Table 7 shows the maximum pressure difference between the hub and shroud for both nozzleless and symmetric configurations. The maximum pressure difference indicates the increasing trend of the centrifugal pressure head for all configurations at both turbine speeds of 30 K rpm and 48 K rpm. At both turbine rotational speeds of 30 K rpm and 48 K rpm, the nozzleless configuration has the lowest maximum pressure difference among all configurations. With the presence of nozzle vanes in the turbine, the centrifugal pressure head increases at both turbine speeds where 48 K rpm has a smaller deviation, of 10%, than 30 K rpm. From the perspective of symmetricity, as the nozzle vane opens from S71L71 to S66L66, the centrifugal pressure head decreases at both turbine speeds of 30 K rpm and 48 K rpm with a deviation of 13% and 11%, respectively. This shows that the influence of opening vane angles on the centrifugal pressure head also has a decreasing trend as the turbine speed increases. In conclusion, the centrifugal pressure head influence does not contribute significantly to secondary flow development as the turbine speed increases, as opposed to the incidence angle effect. However, the symmetricity has a significant impact on the centrifugal pressure head where the centrifugal pressure head increases as the nozzle vane closes from 66° to 71° at both turbine speeds. Meanwhile, as the symmetric nozzle vane closes from 51° to 66°, the symmetricity influence on the centrifugal pressure head is substantial where it decreases at 30 K rpm.

Table 7. Overall configurations result.

Configuration	Rotational Speed (rpm)	Incidence Angle (°)	Maximum Pressure Difference (Pa)	Total to Static Efficiency (%)
Nozzleless	30 K	−12	1048	77.0
	48 K	−37	1345	78.0
S51L51	30 K	−57.9	2690	60.0
	48 K	No experimental data		
S66L66	30 K	−4	1571	70.4
	48 K	−25	1806	74.0
S71L71	30 K	8	1808	68.8
	48 K	−2	2034	72.0

3.2. Off-Design

The off-design performance and understanding of secondary flow structures are exceptionally crucial factors in the design of automobile turbocharger turbines. The rotor encounters significant positive incidence values during off-design operation and engine transients when the turbine is running at low U/C values in the range of 0.3 to 0.5. As a result, the inlet flow is mismatched with the blading, leading to high blade loading, tip leakage, and suction surface separation. These secondary flow structures spread along the blade passage, increasing entropy and resulting in decreased efficiency.

In nozzleless configuration, the peak and minimum efficiency points are recorded at a velocity ratio of 0.6 and 0.4, respectively. As the velocity ratio decreases, a high positive incidence angle occurs where the flow separation tends to dominate at the suction surface. Figure 29 shows the flow topology at a lower velocity ratio for nozzleless configuration. The flow topology at a lower pressure ratio of 0.44 is quite different from the peak efficiency point (PR = 0.78), as illustrated in Figure 13. The flow at the pressure surface has more significant attachment lines with a bigger core of critical points located near the shroud side of the leading edge. The attachment lines start from 0.5 spanwise of the leading edge and extend onto 0.9 spanwise of the trailing edge. The concentration of attachment lines near the shroud is higher than the peak efficiency point. The attachment lines at the hub side also have a high concentration showing a stronger horseshoe vortex. The focus point near the leading edge is more noticeable with a bigger region. It shows significant proof of

a stronger tip leakage vortex than the design point. On the other hand, the flow topology at the suction surface has a completely different flow separation, especially at the leading edge. A significant nodal point is observed at 0.4 spanwise of the leading edge. This happens due to high positive incidence which creates two different locations of attachment lines. One is located near the shroud side that is associated with the tip leakage vortex and the other one is located at the zone near the hub side, which indicates the horseshoe vortex. The concentration of attachment lines is stronger at the hub side than the shroud side. To sum up, the flow separations at both surfaces become stronger with a high concentration of attachment lines and critical points particularly at the suction surface as opposed to the

Figure 29. 30 K rpm flow topology of nozzleless turbine at off-design point.

Theoretically, as the flow topology changes with different flow separations, the entropy generation changes too. The off-design point has a lower efficiency than the peak efficiency point which portrayed higher overall turbine losses. Figure 30 shows the entropy generation at the off-design point for nozzleless configuration. The magnitude of entropy generation at both surfaces increases significantly at the off-design point. On the pressure surface, the entropy generation becomes higher as the flow moves from the leading edge to the trailing edge where the highest entropy generation is spotted at the trailing edge near the hub side. For the suction surface, two regions of high entropy generation are noticeable near the shroud and hub region. The entropy generation at the hub and shroud side indicates the horseshoe vortex and tip leakage vortex, respectively. The maximum pressure difference between the hub and shroud at an off-design point is 2542 Pa.

Figure 30. 30 K rpm entropy generation of nozzleless turbine at off-design point.

With the presence of a symmetric nozzle vane of 66° (S66L66), the peak and minimum efficiency points are recorded at velocity ratio of 0.673 and 0.397, respectively. Figure 31 shows the flow topology of S66L66 at the off-design point. The flow topology for the lower pressure ratio is quite different to the peak efficiency point, especially with the presence of nozzle vanes. The concentration of flow separation at the pressure surface is more pronounced than the suction surface. At the pressure surface, there are distinct attachment lines near the hub and shroud sides. The former attachment lines dominate early streamwise while the latter from the leading to the trailing edge. The attachment line at the shroud side is spread along the blade due to a nodal point spot midstream-wise of 0.9 span. The attachment lines at the hub side, due to the small focus point, also have high concentration showing a stronger horseshoe vortex. However, the nodal point near the

shroud side is more noticeable, with a bigger region than the focus point at the hub side. This is significant proof of a stronger tip leakage vortex than the design point. On the other hand, the flow topology at the suction surface has a completely different flow separation, especially at the trailing edge. A significant separation line is observed at 0.4 spanwise of the trailing edge. In addition, small attachment lines near the shroud side of the trailing edge shows that the tip leakage vortex starts from midstream-wise onwards. The flow topology at the pressure surface with two attachment lines and two critical points are observed at the pressure surface, where it has the focus point and separation lines.
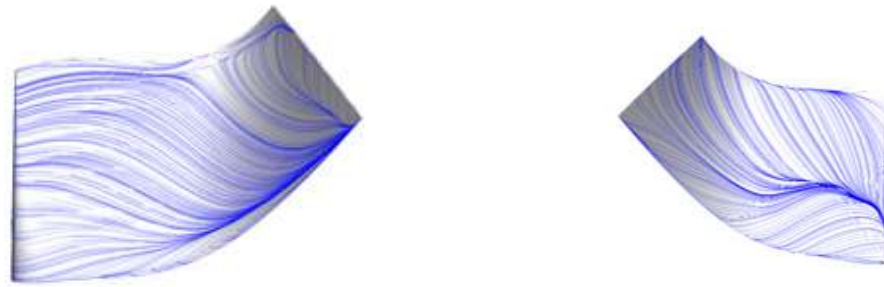

Figure 31. 30 K rpm flow topology of S66L66 at off-design.

Figure 32 shows the entropy generation of S66L66 at the off-design point for 30 K rpm. The magnitude of entropy generation at both surfaces increases significantly at the off-design point. On the pressure surface, the entropy generation becomes higher as the flow enters from the leading edge to the trailing edge, where the highest entropy generation is spotted at the trailing edge near the hub side. For the suction surface, two regions of high entropy generation are spotted near the shroud and hub region. The entropy generation at the hub and shroud side indicates the horseshoe vortex and tip leakage vortex, respectively.
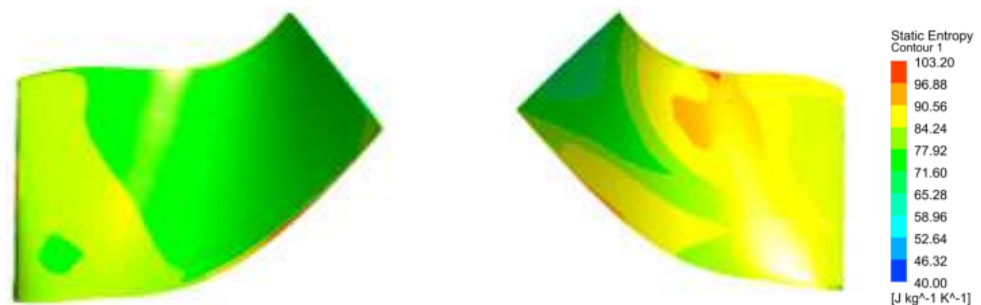

Figure 32. 30 K rpm entropy generation of S66L66 at off-design point.

Where the total to static efficiency disparity between nozzled and nozzleless turbines is substantial, the symmetric opening vane angle has been an essential element influencing overall turbine efficiency, especially in off-design conditions. Figure 33 depicts the change in flow topology as the nozzle vane closes in symmetric configurations at the off-design point. As the nozzle vane opens from S71L71 to S66L66, stronger attachment lines are spotted at the hub and shroud side, with bigger areas of coverage. A nodal point at the tip of the leading edge is observed, too. Because of the strong tip leakage vortex, the attachment lines on the shroud side of the suction surface encompass a larger area. Furthermore, as the nozzle vane opens from S66L66 to S51L51, the number of attachment lines at the pressure surface increases with a larger focus point, and the suction surface attachment lines have extended through the trailing edge.
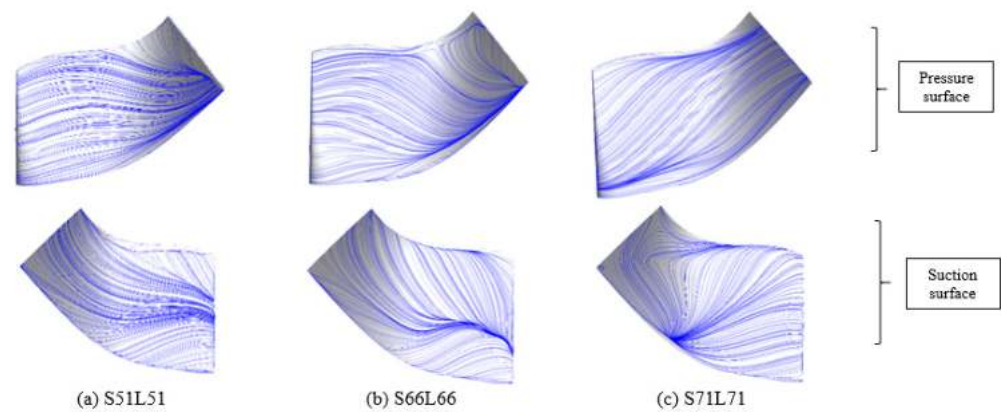
Figure 33. 30 K rpm flow topology for all symmetric configurations at off-design point.

The entropy generation or the losses change due to different flow separations as the opening vane angle changes in off-design conditions as shown in Figure 34. As the nozzle vane opens from S71L71 to S66L66, the entropy generation at both surfaces reduces at both the magnitude and size of the region. In addition, the high entropy generation at the shroud side of the suction surface diminishes. As the nozzle vane opens from S66L66 to S51L51, the area of high entropy generation at the shroud side becomes enormous, with a broader area of high intensity across the surface and the magnitude for both surfaces increasing.
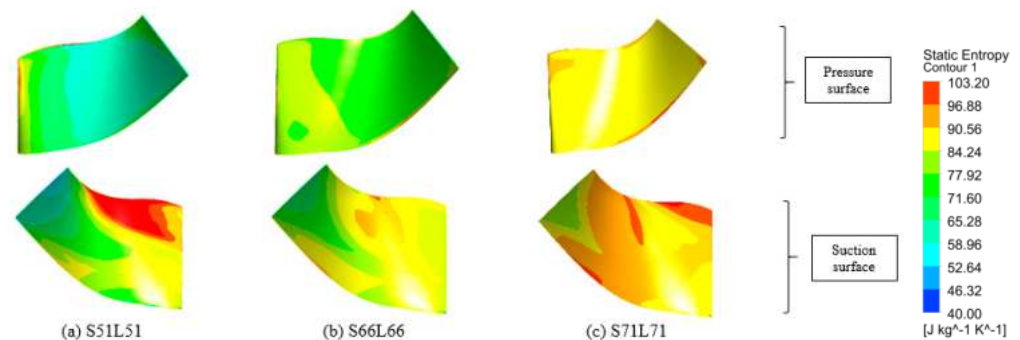

Figure 34. 30 K rpm entropy generation for symmetric configurations at off-design point.

Furthermore, the maximum pressure difference changes as the nozzle vane closes at the off-design point, as shown in Table 8. The centrifugal pressure head decreases as the opening vane angle increases from S71L71 to S66L66, while the centrifugal pressure head increases as the opening vane angle increases from S66L66 to S51L51. This is because S66L66 has the weakest flow separation even at the off-design point, indicating the lowest losses and thus the lowest centrifugal pressure head, whereas S51L51 has the greatest flow separation, indicating a greater number of attachment lines and critical points. S71L71, on the other hand, has mild flow separation that is greater than S66L66 but lower than S51L51. To sum up, the centrifugal pressure head influence on the secondary flow development has a significant impact as the symmetric nozzle vane angle increases.

As the turbine rotational speed increases from 30 K rpm to 48 K rpm, the flow topology for all configurations significantly changes, especially when the turbine is not working in the optimum regime. In the nozzleless configuration, the flow tends to separate on both the suction and pressure surfaces. On the pressure surface, the lower pressure gradient at the leading edge is not as desirable as at 30 K rpm because the intensity of the centrifugal pressure head increases as rotor speed increases. The focus point is noticeable at the leading edge of the shroud side where the attachment lines originate. The friction lines move upwards to combine with the attachment line at the shroud surfaces, demonstrating an occurrence of the tip leakage vortex. At the suction surface, the intensity of the horseshoe vortex at the off-design point is stronger with bigger area coverage near the hub side. There

are two separation lines located near the trailing edge of the 40% blade span where the development of the horseshoe vortex is weaker as turbine speed increases. Attachment lines are also spotted at the shroud side but with weaker intensity than 30 K rpm. As the turbine speed increases from 30 K rpm to 48 K rpm, the flow separation occurs at both surfaces, especially at the suction surface, with a higher number of attachment lines and critical points.

Table 8. Off-design results at both rotational speeds.

Configuration	Rotational Speed (rpm)	Incidence Angle (°)	Maximum Pressure Difference (Pa)	Total to Static Efficiency (%)
S51L51	30 K	−36.1	4184	51.3
	48 K	No experimental data		
S66L66	30 K	16.2	3065	60.4
	48 K	−6.8	3342	71.6
S71L71	30 K	22.7	3302	62.5
	48 K	9.8	3711	54.5

As the symmetric nozzle vane of 66° is introduced at the off-design point, the flow still separates at both suction and pressure surfaces. The attachment lines on both pressure and suction surfaces are still visible but with lower concentration. The number of critical points is reduced to one where a nodal point is only seen at the leading edge of the suction surface.

When the turbine is working at an off-design condition of 30 K rpm, the flow separation of the symmetric nozzle vane is observed at the suction surface as opposed to the nozzleless configuration which separates at both surfaces. The same trend occurs at a higher turbine speed of 48 K rpm but with a lower concentration of attachment lines and critical points.

With the presence of a symmetric nozzle vane at the off-design point, the flow topology at both surfaces changes significantly compared to the nozzleless configuration, which has a greater number of attachment lines and critical points, as shown in Figure 35. However, when the nozzle vanes are introduced into the nozzle interspace at 48 K rpm, the flow tends to split solely at the pressure surface, as opposed to the nozzleless design, where it separates at both the pressure and suction surfaces. In addition, the concentration of flow separation at 48 K rpm is significantly lower than at 30 K rpm with a maximum of two attachment lines, two focus points, and a nodal point found.
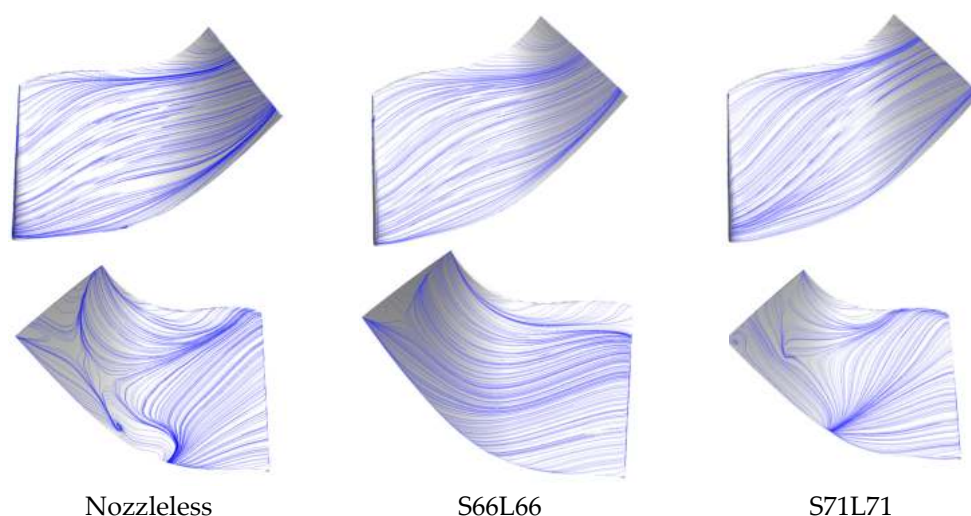

| Nozzleless | S66L66 | S71L71 |

Figure 35. 48 K rpm flow topology in off-design conditions.

In off-design conditions, the influence of symmetricity on the flow separation at both turbine speeds is quite similar to the design point. As the nozzle vane opens from S71L71 to S66L66 at 48 K rpm, the concentration of attachment lines becomes weaker with fewer critical points. At the pressure surface, the attachment lines are thinner than 30 K rpm, while the attachment lines at the suction surfaces become smaller, while the focus point near the leading edge of the pressure surface remains at 30 K rpm and 48 K rpm. Finally, the impact of symmetricity on flow separation is more significant at the off-design point of 30 K rpm, but with less intensity as the turbine speed increases.

Figure 36 show the difference in entropy generation between nozzleless and all symmetric configurations for 48 K rpm in off-design conditions. As the turbine speed increases from 30 K rpm to 48 K rpm in the nozzleless configuration at the off-design point, the magnitude of entropy formation at both the pressure and suction surfaces decreases profoundly. However, the region of high entropy generation is seen on the shroud side of the suction surface only.
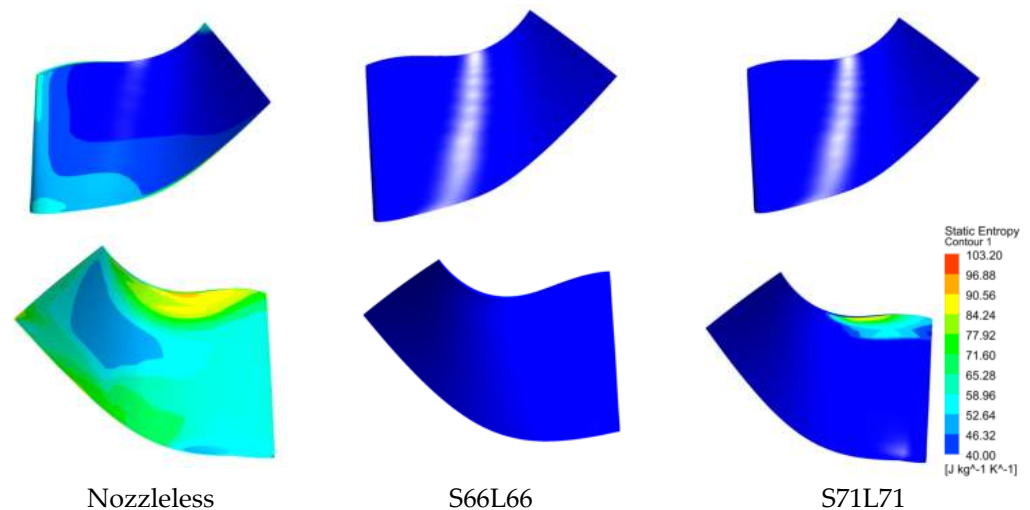

Figure 36. 48 K entropy generation in off-design conditions.

Meanwhile, as the symmetric nozzle vanes of 66° are introduced at the off-design point, lower entropy generation at both pressure and suction surfaces is recorded as the turbine speed increases and the magnitude of entropy generation at the suction surface of a symmetric nozzle vane is much lower than the nozzleless configuration with a smaller region.

As the symmetric nozzle vane closes from S66L66 to S71L71 at an off-design point of 30 K rpm, the region of high entropy generation is spotted at both pressure and suction surfaces, whereas the highest region of entropy generation is located near the shroud side of the suction surface. Additionally, as turbine speed increases, a lower magnitude of entropy generation at both surfaces where the same pattern at 30 K rpm but with lower intensity still occurs. Even at the off-design point, S66L66 still has the lowest magnitude and smallest region of entropy generation among the configurations.

Table 9 shows the maximum pressure difference between the hub and shroud at the off-design point. The maximum pressure difference indicates the centrifugal pressure head has an increasing trend at turbine speeds of 30 K rpm and 48 K rpm for all configurations. The nozzleless configuration has the lowest maximum pressure difference among all configurations for both speeds, even at the off-design point. With the presence of nozzle vanes in both scrolls, the centrifugal pressure head increases at both turbine speeds. However, the deviation at 30 K rpm is 10% higher than at 48 K rpm. From the perspective of symmetricity, as the nozzle vane opens from S71L71 to S66L66, the centrifugal pressure head decreases at both turbine speeds of 30 K rpm and 48 K rpm, with a deviation of 21.6% and 17.7%, respectively. This shows that the influence of opening vane angles on the centrifugal

pressure head also has a decreasing trend as the turbine speed increases. As the turbine works far from the optimum operating regime, the centrifugal pressure head influence still does not contribute a significant impact on the secondary flow development as opposed to the incidence angle for both turbine speeds.

Table 9. Overall configurations result at off-design.

Configuration	Rotational Speed (rpm)	Incidence Angle (°)	Maximum Pressure Difference (Pa)	Total to Static Efficiency (%)
Nozzleless	30 K	7.6	2542	67.7
	48 K	−16.8	4303	62.7
S51L51	30 K	−36.1	8123	51.3
	48 K		No experimental data	
S66L66	30 K	16.2	6141	60.4
	48 K	−6.8	7841	71.6
S71L71	30 K	22.7	7832	62.5
	48 K	9.8	9531	54.5

3.3. Design vs. Off-Design

Since there are two types of configuration, nozzleless and symmetric nozzled configuration, the flow characteristics will be affected. As the boundary conditions indicate the "design" point, peak efficiency is expected as opposed to the "off-design" point. Therefore, a direct comparison between "design" and "off-design" points will be presented.

The flow topology represents the behavior of the flow entering the rotor passage. The intensity of flow separation of nozzleless configuration at the off-design point is stronger at both surfaces, especially at the suction surface where the flow tends to separate there. In addition, the number of critical points is higher at off-design points. A variety of critical points is also spotted at different locations at off-design points as opposed to design points where there is only one type of critical point.

The loss mechanism or entropy generation presented a clear difference between off-design and design points. The magnitude of entropy at the leading edge and shroud side at off-design points is 40% higher than the design point. In addition, the region of high magnitude entropy generation increases for both surfaces at the off-design point.

The centrifugal pressure head is also affected as the turbine is not working in the optimum regime. The maximum pressure difference at the off-design point is higher than double the value at the design point.

As the symmetric nozzle vanes are introduced at the off-design point, the symmetricity influence also changes as opposed to the design point. Three important parameters are used for the analysis: flow topology, entropy generation, and centrifugal pressure head. Firstly, the deviation of flow separation at the off-design point is quite significant compared to the design point. The number of critical points at the off-design point on the symmetricity influence is a bit higher than the design point.

In addition, the entropy generation changes as the turbine works at a lower velocity ratio. The influence of symmetricity on entropy generation is more noticeable at the off-design point. However, a distinct area of high entropy generation is located at the shroud side for both off-design and design points but the magnitude is a bit higher at the off-design.

Moreover, the centrifugal pressure head increases as the turbine speed increases, especially at a low velocity ratio. The deviation of the maximum pressure difference is 40% higher at the off-design point than the design point as shown in Figure 37.

Figure 37. Maximum pressure differences between all configurations at both design and off-design conditions for both turbine speeds.

As the turbine speed increases from 30 K rpm to 48 K rpm, all the parameters also change. The influence of symmetricity on the flow topology at high turbine speed is more noticeable where a higher number of attachment lines and critical points are spotted in off-design conditions. As the nozzle vane opens from S71L71 to S66L66, the intensity of flow separation is stronger at the off-design point than the optimum condition.

As the turbine speed increases, the symmetricity influence on entropy generation almost has the same pattern, but only the magnitude is higher in off-design conditions. For the centrifugal pressure head perspective, the symmetricity influence as turbine speed increases has a similar trend, with a deviation of 5% higher at the off-design point.

4. Conclusions

According to the present study, the development of the secondary flow is significantly influenced by the presence of symmetric nozzle vanes at both scrolls. The presence of nozzle vanes also affects the centrifugal pressure head, especially at high turbine speed. The main conclusions are summarized as follows:

(1)   With the absence of a nozzle vane in an asymmetric double-entry turbine, both tip leakage vortex and horseshoe vortex formed and became dominant at the early stage of the flow going through the rotor passage blade due to the flow separating at both surfaces. The tip leakage vortex evolves along the streamwise plane; however, it peaks at around 50% of the streamwise plane before dropping as a result of boundary layer movement on the pressure surface. Furthermore, the development of a horseshoe vortex becomes substantial at 50% blade chord and gradually weakens along the streamwise plane. By introducing a symmetric nozzle vane for both scrolls, the flow separation seems to occur much more significantly, where the development of the secondary flow is bigger in strength than the nozzleless. The flow also separates at both surfaces of the blade, which deteriorates the turbine efficiency with a higher concentration of attachment lines and more critical points than nozzleless. Moreover, the maximum pressure difference between the hub and shroud indicates centrifugal pressure head for all symmetric configurations is slightly higher than nozzleless. The influence of symmetricity nozzle vane angle on flow separation is more profound compared to nozzleless configuration, with a higher number of critical points and typical patterns at both surfaces. As the nozzle vane closes, the weaker the occurrence of flow separation is at both surfaces. In addition, the least critical points are spotted for both surfaces, especially at the pressure surface. The speedline influence on the flow separation seems to have significant differences for all configurations. As the turbine speed increases, the flow separation becomes weaker and peaks at pressure surfaces for symmetric nozzled configuration, as opposed to nozzleless configuration where it happens at both surfaces. At the off-design point, the same pattern for all influences on flow separation is noticeable but with higher intensity than the peak efficiency point. The number of critical points and attachment lines is significantly higher at the off-design point than the design point.

(2) The entropy generation has different regions and magnitudes for all the configurations. The lowest entropy generation is recorded in the nozzleless configuration at both suction and pressure surfaces. As the symmetric nozzle vane is introduced, the region of entropy generation becomes bigger at the suction surface with a higher magnitude. However, as the symmetric nozzle vane closes, the region of entropy generation becomes smaller and the region focuses on the suction surface only with a lower magnitude. As the turbine speed increases, the entropy generation at both surfaces for all configurations becomes lower, where S66L66 shows the lowest entropy generation with the smallest region of high entropy. At the off-design point, the same pattern is observed for all influences where the speedline influence shows a lower intensity than the symmetricity influence. The magnitude of high entropy generation is noticeable in off-design conditions with a bigger area of high entropy generation at both surfaces than the design point.

(3) The maximum difference in pressure between the shroud and hub is inversely proportional to the turbine efficiency for both nozzleless and symmetric configurations, either at off-design or peak efficiency points. However, as the turbine speed increases, the centrifugal pressure head also increases. The nozzleless configuration has the lowest maximum pressure difference, which indicates the lowest centrifugal pressure head among all configurations at both turbine speeds of 30 K rpm and 48 K rpm. As the symmetric nozzle vane is introduced, the maximum pressure difference increases and decreases as the nozzle vane closes from S51L51 to S66L66 and from S66L66 to S71L71, respectively. As turbine speed increases, the influence of symmetricity is quite similar, with a 2% difference between 30 K rpm and 48 K rpm deviation. At lower velocity ratio conditions, a higher centrifugal pressure head is observed for all configurations. In addition, the difference in the intensity at off-design is more noticeable with higher magnitude than the design point for all influences, such as the introduction of symmetric nozzle vanes, symmetricity of nozzle vanes, and rotational speed.

In conclusion, the maximum pressure difference that indicates the centrifugal pressure head influence is one of the important factors that needs to be reduced, which can increase the overall turbine efficiency by minimizing the secondary flow development in the rotor passage blade.

Author Contributions: Methodology, B.A.G.; Software, U.K.; Validation, B.A.G.; Writing—original draft, M.J.A.J. and B.A.G.; Supervision, B.A.G. and R.M.B. All authors have read and agreed to the published version of the manuscript.

Conflicts of Interest: The authors declare no conflict of interest.

References

1. Newton, P.J. An Experimental and Computational Study of Pulsating Flow within a Double Entry Turbine with Different Nozzle Settings. Ph.D. Thesis, Imperial College London, London, UK, 2013.
2. Natkaniec, C.K.; Kammeyer, J.; Seume, J.R. Secondary flow structures and losses in a radial turbine nozzle. In *Turbo Expo: Power for Land, Sea, and Air*; 2011; Volume 54631, pp. 977–987.
3. Chen, L.; Zhuge, W.; Zhang, Y.; Zhang, S.; Zhang, J. Investigation of the secondary flow structure in the mixed flow turbine for a high pressure ratio turbocharger. *Proc. ASME Turbo Expo* **2008**, *43161*, 1611–1618.
4. Yang, B.; Newton, P.; Martinez-Botas, R. Understanding of secondary flows and losses in radial and mixed flow turbines. *J. Turbomach.* **2020**, *142*, 081006. [CrossRef]
5. Sajedin, A.; Fard, M.H.S.; Khalkhali, A. Radial gradient pressure effects on flow behavior in a dual volute turbocharger turbine. *Appl. Sci.* **2018**, *8*, 1961. [CrossRef]
6. Baum, O.; Koschichow, D.; Frohlich, J. Influence of the coriolis force on the flow in a low pressure turbine cascade T106. *Proc. ASME Turbo Expo* **2016**, *49705*, V02BT38A044.
7. Putra, M.A.; Joos, F. Investigation of secondary flow behavior in a radial turbine nozzle. *J. Turbomach.* **2006**, *135*, 061003. [CrossRef]

8.   Feng, Z.; Sun, R.; Cui, W.; Xu, J. Research on Effects of Incidence to Turbine Guide Cascade Aerodynamic Performance. *Teh. Vjesn.* **2019**, *3651*, 736–742.

9.   Horlock, J.H.; Lakshminarayana, B. Secondary Flows: Theory, Experiment, and Application in Turbomachinery Aerodynamics. *Annu. Rev. Fluid Mech.* **1973**, *5*, 247–280. [CrossRef]

10. Ketata, A.; Driss, Z.; Abid, M.S. Impact of blade number on performance, loss and flow characteristics of one mixed flow turbine. *Energy* **2020**, *203*, 117914. [CrossRef]

11. Yang, B. Secondary Flows and Unsteady 1D Modelling on Centripetal Turbine. Ph.D. Thesis, Imperial College London, London, UK, 2019.

12. Marsan, A.; Moreau, S. Analysis of the flow structure in a radial turbine. In Proceedings of the 11th European Conference on Turbomachinery Fluid Dynamics & Thermodynamics, ETC 2015, Madrid, Spain, 23–27 March 2015.

13. Palfreyman, D.; Martinez-Botas, R.F. Numerical study of the internal flow field characteristics in mixed flow turbines. *Am. Soc. Mech. Eng. Int. Gas Turbine Inst. Turbo Expo IGTI* **2002**, *5*, 455–472.

14. Fan, H.; Ni, J.; Wang, H.; Zhu, Z.; Liu, Y. *Numerical Study of Unsteady Performance of a Double-Entry Turbocharger Turbine under Different A/R Value Conditions*; SAE Technical Paper: Warrendale, PA, USA, 2016.

15. Ciorciari, R.; Schubert, T.; Niehuis, R. Numerical investigation of secondary flow and loss development in a low-pressure turbine cascade with divergent endwalls. *Int. J. Turbomach. Propuls. Power* **2018**, *3*, 5. [CrossRef]

16. Newton, P.; Martinez-Botas, R.; Seiler, M. A Three-dimensional computational study of pulsating flow inside a double entry turbine. *J. Turbomach.* **2015**, *137*, 031001. [CrossRef]

17. Lin, D.; Yuan, X.; Su, X. Local entropy generation in compressible flow through a high pressure turbine with delayed detached eddy simulation. *Entropy* **2017**, *19*, 29. [CrossRef]

18. Zhang, Q.; Du, J.; Li, Z.; Li, J.; Zhang, H. Entropy Generation Analysis in a Mixed-Flow Compressor with Casing Treatment. *J. Therm. Sci.* **2019**, *28*, 915–928. [CrossRef]

19. Simpson, A.T.; Spence, S.W.T.; Watterson, J.K. A comparison of the flow structures and losses within vaned and vaneless stators for radial turbines. *J. Turbomach.* **2009**, *131*, 1–15. [CrossRef]

20. Feneley, A.J.; Pesiridis, A.; Andwari, A.M. Variable Geometry Turbocharger Technologies for Exhaust Energy Recovery and Boosting-A Review. *Renew. Sustain. Energy Rev.* **2017**, *71*, 959–975. [CrossRef]

21. Capobianco, M.; Gambarotta, A. Variable geometry and waste-gated automotive turbochargers: Measurements and comparison of turbine performance. *J. Eng. Gas Turbines Power* **1992**, *114*, 553–560. [CrossRef]

22. Serrano, J.R.; Piqueras, P.; De la Morena, J.; Gómez-Vilanova, A.; Guilain, S. Methodological analysis of variable geometry turbine technology impact on the performance of highly downsized spark-ignition engines. *Energy* **2021**, *215*, 119122. [CrossRef]

23. Dasgupta, S.; Sarmah, P.; Borthakur, P.P. Application of variable geometry turbine turbochargers to gasoline engines-A review. *IOP Conf. Ser. Mater. Sci. Eng.* **2020**, *943*, 012010. [CrossRef]

24. Kreckel, K.; Croxall, K.; Kreckel, K.; Platen, E.; Chen, C.; Lin, J. Impact by double scroll on variable geometry turbine performance. *J. Phys. Conf. Ser.* **2022**, *2217*, 012082.

25. Martinez-Botas, R.; Sakai, M. Asymmetric Double Entry Turbine. Ph.D. Thesis, Imperial College London, London, UK, 2014.

26. Gurunathan, B. Experimental Evaluation of Steady and Pulsating Flow Performance of an Asymmetric Double Entry Turbine for an Automotive Turbocharger. Ph.D. Thesis, Imperial College London, London, UK, 2017.

27. Gurunathan, B.A.; Khairuddin, U.; Nabill, N.; Shah, A.; Martinez, R. Influence of Double Entry Volute on Incidence Angle Variation Under Steady Flow: Numerical Investigation. *CFD Lett. J.* **2020**, *10*, 75–89. [CrossRef]

28. Padzillah, M.H.; Rajoo, S.; Martinez-Botas, R.F. Numerical assessment of unsteady flow effects on a nozzled turbocharger turbine. *Proc. ASME Turbo Expo* **2012**, *8*, 745–756.

29. Rajoo, S. Steady and Pulsating Performance of a Variable Geometry Mixed Flow Turbocharger Turbine. Ph.D. Thesis, Imperial College London, London, UK, 2007; p. 294.

30. Abidat, M.; Baines, N.C.; Firth, M.R. Design of a Highly Loaded Mixed Flow Turbine. *Proc. Inst. Mech. Eng. Part A J. Power Energy* **1992**, *206*, 95–107. [CrossRef]

31. Palfreyman, D.; Martinez-Botas, R.F. The pulsating flow field in a mixed flow turbocharger turbine: An experimental and computational study. *J. Turbomach.* **2005**, *127*, 144–155. [CrossRef]